

Andreas Vogel¹

Atmospheric and Climate Department,
Norwegian Institute for Air Research,
Kjeller 2027, Norway;
Department of Geoscience,
University of Oslo,
Oslo 0316, Norway
e-mail: vogel.avo@gmail.com

Adam J. Durant

Satavia Ltd.,
Cambridge CB4 3AZ, UK;
Geological and Mining Engineering
and Sciences,
Michigan Technological University,
Houghton, MI 49931
e-mail: adam.durant@satavia.com

Massimo Cassiani

Atmospheric and Climate Department,
Norwegian Institute for Air Research,
Kjeller 2027, Norway
e-mail: massimo.cassiani@nilu.no

Rory J. Clarkson

Rolls-Royce plc.,
Engine Environmental Protection,
Derby DE24 9HX, UK
e-mail: rory.clarkson@rolls-royce.com

Michal Slaby

Rolls-Royce plc.,
Installation Aerodynamics,
Derby DE24 9HX, UK
e-mail: michal.slaby@rolls-royce.com

Spyros Diplas

SINTEF-Industry,
Oslo 0314, Norway
e-mail: spyros.diplas@sintef.no

Kirstin Krüger

Department of Geoscience,
University of Oslo,
Oslo 0315, Norway
e-mail: kirstin.kruger@geo.uio.no

Andreas Stohl

Atmospheric and Climate Department,
Norwegian Institute for Air Research,
Kjeller 2027, Norway
e-mail: andreas.stohl@nilu.no

Simulation of Volcanic Ash Ingestion Into a Large Aero Engine: Particle–Fan Interactions

Volcanic ash (VA) clouds in flight corridors present a significant threat to aircraft operations as VA particles can cause damage to gas turbine engine components that lead to a reduction of engine performance and compromise flight safety. In the last decade, research has mainly focused on processes such as erosion of compressor blades and static components caused by impinging ash particles as well as clogging and/or corrosion effects of soft or molten ash particles on hot section turbine airfoils and components. However, there is a lack of information on how the fan separates ingested VA particles from the core stream flow into the bypass flow and therefore influences the mass concentration inside the engine core section, which is most vulnerable and critical for safety. In this numerical simulation study, we investigated the VA particle–fan interactions and resulting reductions in particle mass concentrations entering the engine core section as a function of particle size, fan rotation rate, and for two different flight altitudes. For this, we used a high-bypass gas-turbine engine design, with representative intake, fan, spinner, and splitter geometries for numerical computational fluid dynamics (CFD) simulations including a Lagrangian particle-tracking algorithm. Our results reveal that particle–fan interactions redirect particles from the core stream flow into the bypass stream tube, which leads to a significant particle mass concentration reduction inside the engine core section. The results also show that the particle–fan interactions increase with increasing fan rotation rates and VA particle size. Depending on ingested VA size distributions, the particle mass inside the engine core flow can be up to 30% reduced compared to the incoming particle mass flow. The presented results enable future calculations of effective core flow exposure or dosages based on simulated or observed atmospheric VA particle size distribution, which is required to quantify engine failure mechanisms after exposure to VA. As an example, we applied our methodology to a recent aircraft encounter during the Mt. Kelud 2014 eruption. Based on ambient VA concentrations simulated with an atmospheric particle dispersion model (FLEXPART), we calculated the effective particle mass concentration inside the core stream flow along the actual flight track and compared it with the whole engine exposure.

[DOI: 10.1115/1.4041464]

1 Introduction

The aviation industry deals with various atmospheric environmental threats on a daily basis and judges their potential hazard to aircraft and gas turbine engine operations including schedule delays, cancellations, and occasionally safety. One of these

aviation threats is airborne volcanic ash (VA) [1–3]. Volcanic ash is the smallest fraction of tephra (solid erupted material) with a diameter of less than 2 mm and is formed during explosive or phreatomagmatic volcanic eruptions when dissolved gases in magma expand or interact with water and are released violently into the atmosphere [4].

Volcanic eruptions can be energetic enough to emit VA and gases into the mid and upper troposphere and even into the stratosphere [5]. While the coarse fraction of volcanic ash ($63 \mu\text{m} < \text{diameter} < 2000 \mu\text{m}$) is quickly removed from the

¹Corresponding author.

Manuscript received March 4, 2018; final manuscript received September 8, 2018; published online November 12, 2018. Assoc. Editor: Rakesh Srivastava.

atmosphere by gravitational settling, its fine fraction ($< 63 \mu\text{m}$ in diameter) can remain airborne for several hours and up to weeks [4]. Thus, depending on the eruption column height, injected particle size distributions and atmospheric dynamics (three-dimensional wind direction and wind strength), VA particles can be transported by the atmospheric circulation hundreds to thousands of kilometers downstream from the source of the eruption [6] and are typically found in thin layers in the atmosphere. Given that major aviation flight routes intersect the world's most active volcanic regions [7], these VA layers can affect commercial air traffic routes significantly [2,8].

How severe VA clouds in flight corridors can be for global air traffic, was illustrated by the 2010 Icelandic Eyjafjallajökull eruption. Although the eruption was relatively small ($\sim 11 \text{Tg}$ of fine ash particles were injected into the midtroposphere [9]), the presence of VA in flight corridors forced authorities to impose flight restrictions and re-routing during a full airspace closure, leading to large economic and societal impacts with estimated losses of US\$5.5b globally [10]. Even though the eruption emphasized the problem VA poses to flight operations, particularly in a geographic region (i.e., Europe) with a very dense network of flight routes, the threat of VA particles to aviation was already known in both science and in the industry for many years.

Over the past century, there have been a considerable number of aircraft encounters with various drifting volcanic ash clouds [11]. Between 1953 and 2009, 129 incidents were reported, resulting in several hundreds of million US\$ of aircraft and engine damage. Considering that presumably not all encounters have been reported in the past decades, the real number of aircraft encounters and the associated costs might be significantly higher [12]. Two notable aircraft encounters are those of British Airways Flight 9 over Java (Mt. Galunggung eruption) in 1982 and KLM Flight 867 over Alaska (Redoubt eruption) in 1989. Both flights experienced multi-engine failures including the in-flight shutdown of all four engines (following engine surge) after flying through thick VA clouds with estimated peak concentrations between 100mg/m^3 and 2000mg/m^3 for several minutes at a distance of 250–1000 km from the eruption source [13–15]. After the significant loss of performance on the engines, and descending several thousand feet out of the ash cloud, in both cases the pilots managed to restart the engines and gain sufficient power to safely land the aircraft [13]. However, the potential threat to safe flight operations was obvious.

A more recent reported encounter was the Jet Star Flight 114 over Indonesia (Mt. Kelud eruption) in 2014. In contrast to the two previously described cases, this encounter did not cause any immediate engine failures, but concerns over the consequence of the encounter were enough that both engines had to be taken off the wing and replaced after the incident. The eruption went on for only a few days (and only the first few hours were extremely energetic), but the fine ash fraction of the erupted material was detected in the atmosphere (lower stratosphere) up to 3 months after the eruption [16]. The encounter happened right after the highest volcanic activity. Postflight analysis showed that the aircraft was flying in atmospheric VA concentrations of around 2mg/m^3 for approximately 10 min before the pilots managed to escape the ash plume (dosage of $1.2 \pm 0.3 \text{g/m}^3$) [17]. Engine inspections indicated only minor signs of deteriorations of engine parts.

Volcanic ash particles consist of fragmented rocks, different minerals (e.g., feldspars, silicates, olivine) and volcanic glass. Once injected into the engine, VA particles have the potential to produce both short-term and long-term damage leading to a reduction in engine performance and component lifetime, as well as unscheduled maintenance and repair costs. Because of their non-spherical and angular shapes [18,19], VA particles are highly abrasive. This leads to erosion of forward facing surfaces (fan, compressor blades, and fuel spray nozzles) during their transition through the engine (mainly fan and compressor stages), which leads to a loss of compressor aerodynamic efficiency [20–22].

Furthermore, after entering the engine's hot section (combustor and high pressure turbine stages), the particles undergo a phase transition [23] and can become plastic [13] based on their lower phase transition temperature (about $650\text{--}1000^\circ\text{C}$ depending on igneous rock type) compared to the operating temperature of the individual engine stages ($1400\text{--}1800^\circ\text{C}$). Consequently, ash particles deform while they become soft, semisolid viscous material or even melt in the hot section and can adhere onto combustor liners, fuel spray nozzles, and high-pressure nozzle guide vanes [24]. In the case of high-pressure nozzle guide vane adhesion, the soft (semisolid) or molten VA particles can resolidify on the vanes, which have a lower temperature than the particles. The resolidified material on the surface leads to clogging of cooling holes (overheating of components) [25], to chemical reaction (corrosion) or infiltrations of the thermal-barrier coating layer around the vanes [26–28] (Calcium, Magnesium, Aluminum, Silica—CMAS—attack). This also leads to an aerodynamic reduction or blockage of the internal throat area between vane airfoils due to material build-up (accretion), which alters the critical safety surge margins and leads to a loss of controllable thrust.

Engine system degradation, damage, and failure mechanisms depend to a large extent on their VA exposure dosage [15], but are also influenced by the physical and chemical properties of VA particles [29]. The engine dosage is defined as the mass of volcanic ash an engine will be exposed to (engine ingestion concentration) and the duration of exposure [30]. However, the exposure dosage that is relevant for the engine core section susceptibility is not the total mass of VA the engine is exposed to but the mass inside the engine core flow. The relationship between particle mass flow at the engine intake and the core stream flow depends on the bypass ratio of the engine and particle–fan interactions. The interactions depend on the size distribution of ingested particles as well as engine parameters such as particle separation efficiencies by the fan. Whereas the size distribution of VA particles in the atmosphere has been studied extensively, only a little information is available on the influence of the turbofan on the ingestion of particles into the engine core section [21,31].

It is hypothesized that the fan acts like an ash particle separator for the entire engine depending on the ingested particle size and flight conditions (i.e., true airspeed and rotating speed of the fan), where particles with a low Stokes number ($\text{Stk} \ll 1$) move along the main air flow and pass through the fan. Therefore, the $\text{Stk} \ll 1$ particle fraction does not have any interaction with fan surfaces and is directly ingested into the core stream flow. In contrast, particles with a large Stokes number ($\text{Stk} \gg 1$) have large inertia and detach from the mean flow trajectories [32]. Once detached, these particles can collide with fan surfaces and, depending on the impact forces and impact angle, be centrifuged out of the core stream flow into the bypass stream flow (Figs. 1 and 2). Thus, the particle–fan interactions have a direct impact on the particle size distribution and consequently on the resulting particle mass concentration entering the engine core section, which is the most critical part of the engine for air safety. A better quantitative understanding is needed on how VA particles of different sizes interact with the fan and how this modifies the incoming VA particle size distribution and total VA mass entering the core section. The improved understanding would lead to reduced uncertainties of mass concentrations needed to relate relevant VA concentrations to potential engine failure mechanisms such as erosion, adhesion, or secondary air system contaminations.

In this paper, we perform computational fluid dynamics (CFD) simulations of volcanic ash particle-laden airflows entering a high-bypass gas-turbine engine of simplified design, but with representative intake, fan, spinner, and splitter geometries. This setup allows us to study VA particle–fan interactions and particle trajectories after surface impact as well as to calculate the change of particle size distribution inside the core stream flow. Finally, we use the resulting VA mass concentration reduction for the modeled data along the real flight track of the above-mentioned Mt. Kelud encounter as a case study.

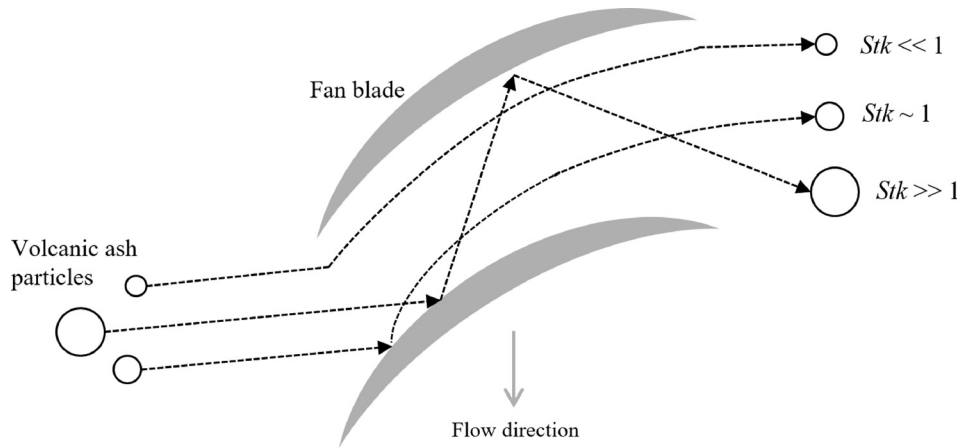


Fig. 1 Particle trajectories of VA particles in the simulations: (a) particles with $Stk \ll 1$ follow closely streamlines of the gas-phase flow and have no or limited contact with the fan surface and (b) particles with $Stk \gg 1$ are dominated by their inertia and detach from the gas-phase flow streamlines, leading to partial or full surface contact

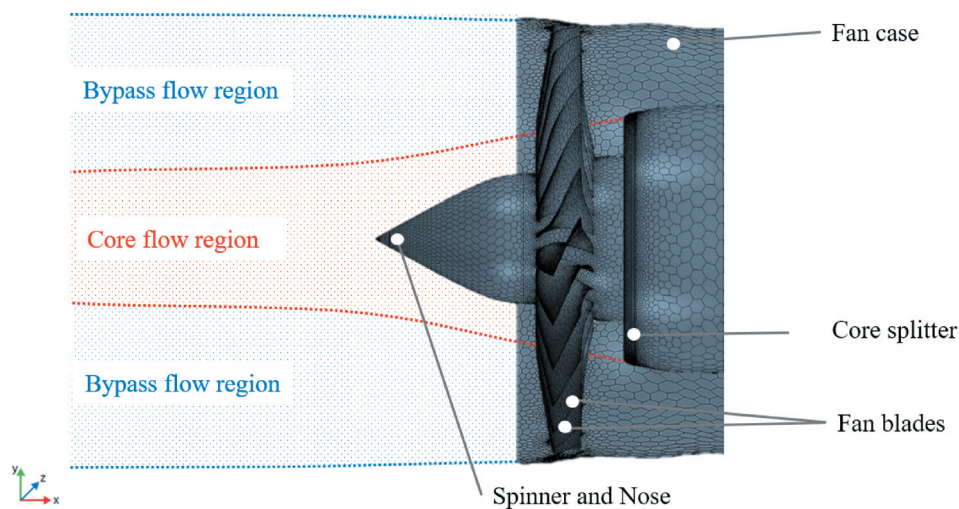


Fig. 2 Main engine geometry parts used for the numerical CFD experiments, i.e., the fan with 26 single blades, spinner and nose, fan case and core splitter, including the bypass flow region (blue shaded area) and the core flow region (red shaded area). Furthermore, the shown cells on the main geometry parts illustrate the polyhedral mesh structure.

2 Methods

The workflow for the particle-tracking simulation experiments (Fig. 3) involves: (1) engine geometry review, preparation, and discretization into a polyhedral three-dimensional mesh including prism layers (preprocessing), (2) simulation of the three-dimensional flow fields generated under different fan rotation rates and different atmospheric conditions (processing) and (3) simulation of VA particle ingestion into the engine and their interaction with fan surfaces (Postprocessing). All working steps were performed using a commercial CFD suite (STAR-CCM+ version 11.06 [33]) that was originally designed for solving multidisciplinary problems in both fluid and solid continuum mechanics, within a single integrated user interface.

2.1 Engine Geometry Preparation and Discretization (Preprocessing). We used a high-bypass ratio gas-turbine engine design, with representative straight intake, fan, spinner, and splitter geometries used on current in-service wide-bodied aircraft, provided by Rolls-Royce. The modeled engine type is used for medium and long-haul operations and has accrued millions of civil and cargo in-service flight hours. The engine type is

representative of many related engine types in service today. The engine geometry is a simplified, but representative engine reproduction and consists of a fan stage with 26 single blades (including rounded leading edges) and nose/spinner, a fan casing and a core splitter and an intake.

After preparation of the engine computer-aided design files, we defined the computational domain and constructed the numerical mesh. The individual geometry parts were discretized into finite volume cells, where they were first transformed into a two-dimensional surface mesh using Delaunay triangulation [34] and subsequently into a three-dimensional volume mesh by converting triangles into unstructured tetrahedral cell shapes. Based on the resulting tetrahedral cells, we used a STAR-CCM+ specific dualization scheme to create an arbitrary polyhedral mesh from the underlying tetrahedral mesh. This resulted in higher accuracy and fewer cells as well as a better grid convergence compared to tetrahedral meshes [35], which reduced computational time (Fig. 2). In addition to the volume mesh, we applied local surface and volumetric refinements, where appropriate and to leading and trailing edges of all blades as well as to forward facing surfaces (i.e., intake, splitter, nose tip). Furthermore, we included four layers of orthogonal prismatic cells (prism layers) with y^+ values ~ 1 next

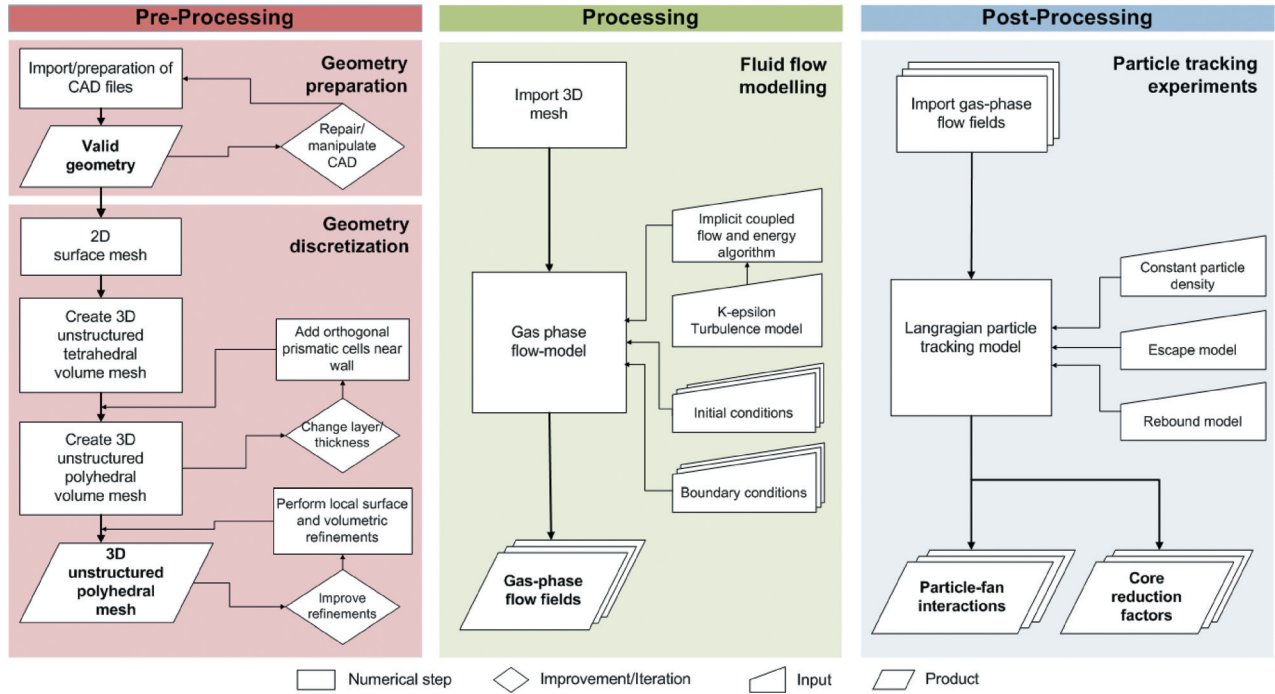


Fig. 3 Workflow for the particle-tracking experiments including engine geometry review, preparation, and discretization (pre-processing), simulation of the three-dimensional flow fields (Processing) and simulation of particle trajectories inside the engine (postprocessing)

to the wall boundaries in the volume mesh to better reproduce turbulent heat and momentum transfer near the walls. The complete computational domain consists of 1.15×10^7 polyhedral cells, 7.45×10^7 faces and 6.29×10^7 vertices.

2.2 Numerical Setup (Processing). For the particle tracking experiments, we assumed that the VA particles move isolated and therefore have no influence on the gas-phase flow and no interactions between each other (one-way coupling regime). This is justified by the large inter-particle spacing (>100), that can be calculated from

$$\frac{L}{D_p} = \left(\frac{\pi}{6\alpha_p} \right)^{\frac{1}{3}} \quad (1)$$

where L is the average distance between the centers of two particles, D_p is the diameter of the VA particles and α_p is the volume fraction of the dispersed phase in air (assumed maximum mass concentration of 4 mg/m^3 and a maximum diameter of $200 \mu\text{m}$) [36]. This assumption allowed us to separate the numerical experiments into two computational steps, (1) simulation of the gas-phase flow to determine representative and robust steady-state flow fields, and (2) particle-phase simulation by means of a stochastic Lagrangian particle-tracking model.

2.2.1 Gas-Phase Flow Including Two-Equation Turbulence Model. For the determination of the three-dimensional gas-phase flow, we used an implicit-coupled flow and energy algorithm including a two-equation turbulence model. The flow and energy multigrid algorithm provides an accurate solution for compressible flows, particularly in the presence of rapid changes of flow conditions from subsonic to transonic flow conditions (shocks). It solves the governing equations for the conservation of mass

$$\frac{\partial \rho_g}{\partial t} + \frac{\partial}{\partial x_i} (\rho_g u_i) = 0 \quad (2)$$

conservation of momentum (Reynolds-averaged Navier–Stokes equations of motion)

$$\frac{\partial}{\partial t} (\rho_g u_i) + \frac{\partial}{\partial x_i} (\rho_g u_i u_j + p \delta_{ij}) = \rho_g f_i \quad (3)$$

and conservation of energy

$$\frac{\partial}{\partial t} (\rho_g E) + \frac{\partial}{\partial x_i} \left[\rho_g u_i \left(E + \frac{p}{\rho_g} \right) - \tau_{ij} u_i + q_i \right] = \rho_g f_i u_i \quad (4)$$

simultaneously assuming a steady-state ($\partial/\partial t = 0$). This is achieved by using a pseudo-time marching scheme considering a constant Courant number (time steps are locally determined) and constant von Neumann stability conditions. Furthermore, the algorithm includes a second-order Gauss–Seidel relaxation upwind scheme for the discretization of the convection terms in the momentum transport equation (second term on the left-hand side in Eq. (3)) and flow boundary diffusion in the energy equation (implicit spatial integration for steady-state analysis, second term on the left-hand side in Eq. (4)). In the above equations, t is the local time, x_i is the particle position, ρ_g is the gas-phase density, u_i is the flow velocity, E is the total energy, q_i is the heat flux, f_i is the external energy sources, τ_{ij} is the Kronecker delta (function of variable i, j), and τ_{ij} is the total stresses (molecular and Reynolds stresses). Relations between the internal fluid energy and density (thermodynamic relationships of the conservation equations), were realized by the use of the ideal gas law, where the density is expressed as a function of gas temperature (T) and gas pressure (p), $\rho_g = p/RT$ (R is the specific gas constant of air).

In order to close the governing flow equations, we used a two-equation turbulence model to define the turbulent Reynolds stresses and the heat fluxes. The applied turbulence model was a realizable $k-\varepsilon$ (RKE) eddy-viscosity model for high Reynolds number turbulent gas flows [37]. The RKE model solves for two variables, the turbulent kinetic energy (k), and the turbulent dissipation rate (ε) to calculate the turbulent viscosity

$$\mu_t = \rho_g C_\mu f_\mu k T_e \quad (5)$$

where C_μ is the model function of the RKE, f_μ is the damping function, and T_e is the large-eddy turbulence time scale ($T_e = k/\varepsilon$). The turbulent transport equations for k and ε are defined as

$$\begin{aligned} \frac{\partial}{\partial t}(\rho_g k) + \frac{\partial}{\partial u_i}(\rho_g k u_i) \\ = \frac{\partial}{\partial x_i} \left[\left(\mu_g + \frac{\mu_t}{\sigma_k} \right) \frac{\partial k}{\partial u_i} \right] + P_k - \rho_g(\varepsilon - \varepsilon_0) + S_k \end{aligned} \quad (6)$$

$$\begin{aligned} \frac{\partial}{\partial t}(\rho_g \varepsilon) + \frac{\partial}{\partial u_i}(\rho_g \varepsilon u_i) \\ = \frac{\partial}{\partial x_i} \left[\left(\mu_g + \frac{\mu_t}{\sigma_\varepsilon} \right) \frac{\partial \varepsilon}{\partial u_i} \right] + \frac{1}{T_e} C_{\varepsilon_1} P_\varepsilon - C_{\varepsilon_2} f_2 \rho_g \left(\frac{\varepsilon}{T_e} - \frac{\varepsilon_0}{T_0} \right) + S_\varepsilon \end{aligned} \quad (7)$$

where μ_g is the dynamic gas-phase viscosity, σ_ε , C_{ε_1} , and C_{ε_2} are model coefficients, P_k and P_ε are the turbulent kinetic energy and the dissipation rate production terms, respectively, f_2 is a damping function, and S_k as well as S_ε are source terms for the kinetic energy and turbulent dissipation rate. In the RKE, the model coefficients in the eddy viscosity and transport equations (Eqs. (5)–(7)) are computed dynamically as a function of the mean gas flow and turbulence properties. A more detailed description of the above-given equations and the coefficients of the RKE can be found in Ref. [37]. The RKE model has been implemented in STAR-CCM+ with a two-layer approach [38], which activates the coefficients to be used with fine meshes that also resolve the viscous sublayer (important especially around the airfoils).

The rotation of the fan blades in this setup is realized by the use of a moving reference frame (MRF), which is a robust and efficient approach to simulate rotating motion in steady-state turbomachinery solutions. In this approach, the positions of the cell vertices do not change in space, but the two regions, i.e., the stationary and the rotating region (includes the fan and the spinner) are connected with an internal indirect interface (mixing plane) with no gaps between the static and rotating region (aligned on the same axis). The two regions, or frames, rotate relative to each other and transfer circumferentially averaged flow properties across the interface (transfer of mass, momentum, energy, and other conserved quantities). In the MRF, the absolute Cartesian rotation velocity components are calculated, using the flux relative to the rotation of the local frame of reference (nonrotating)

$$\nabla \cdot (\mathbf{u}_R \times \mathbf{u}_I) + \boldsymbol{\Omega} \times \mathbf{u}_I = \nabla \left(\frac{p}{\rho_g} \right) + \nu \quad (8)$$

where ω is the rotation (acceleration) term in the rotation frame, u_R is the rotating velocity u_I the inertial velocity, and ν is the kinematic viscosity. In our setup, the stationary region includes the intake, inner engine case, and the core splitter, whereas the rotating region includes the fan, the spinner, and the nose. Figure 4 shows exemplarily the rotating vectors of the MRF, including the fan and spinner parts, for an example, fan speed.

2.2.2 Lagrangian Particle Model. For the calculation of the particle trajectories, we used a stochastic Lagrangian particle-tracking model. The model calculates the translational force balance and rotational momentum balance of VA particles as well as their turbulent velocity fluctuations. As mentioned earlier, the influence of particles acting on the gas-phase flow and effects such as particle–particle interaction was neglected due to the one-way coupling regime ($L/D_p > 100$). Hence, the Eulerian gas-phase flow fields are fixed (or frozen), and the translational force balance can be calculated as the particle acceleration

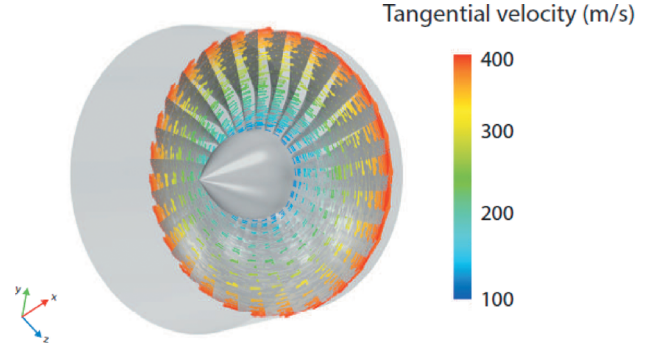


Fig. 4 Moving reference frame (gray cylinder) including fan and spinner for an example of medium fan power condition. The tangential velocity increases significantly from the hub to the tip of the rotor blade and reaches velocities around Mach numbers ~ 1 .

($d/dt)(dx_p/dt)$, where x_p is the particle position described as a function of particle velocity (u_p) and time (t), and the sum of the main external forces ($f_{p,i} = F/m_p$) acting on the particle

$$\frac{d}{dt} u_p = \sum f_{p,i} \quad (9)$$

where $m_p = \rho_p D_p^3 \pi / 6$ is the mass of a particle (ρ_p is the particle density and D_p the particle diameter). $f_{p,i}$ represents all external forces acting on the particle. In this setup, $f_{p,i}$ is the sum of the specific drag force ($f_{p,d}$), gravitational force ($f_{p,g}$), specific pressure force ($f_{p,p}$), and additional external forces exerted by the moving reference frame ($f_{p,MRF}$). All other forces are neglected. The specific drag force

$$f_{p,d} = \beta_p (u_g - u_p) \quad (10)$$

is based on the difference of the gas-phase velocity (u_g) and the particle velocity (u_p) and the interphase drag coefficient [39]

$$\beta_p = \alpha_g \frac{18 \mu_g C_D \text{Re}_p}{\rho_p D_p^2 24} \quad (11)$$

In the above equation, α_g denotes the volume fraction of the gas-phase, μ_g is the viscosity of the gas-phase, Re_p is the particle specific Reynolds number, and C_D is the drag coefficient. Following the correlation by Schiller and Naumann [40], the drag coefficient was assumed to be constant ($C_D = 0.44$), as the particle Reynolds number ($\text{Re}_p = \rho_g d_p |u_g - u_p| / \mu_g$) was calculated to be $\text{Re}_p > 1000$ (Newton's Law). The particle acceleration due to gravity ($f_{p,g} = m_p g$) was included in the calculations, although its influence is only marginal due to high axial particle velocity. The pressure force ($f_{p,p}$) was considered as the negative proportion of the pressure gradient (∇p), and the fluid density as a result of the gas-phase flow and the particle acceleration inside the engine intake stream flow

$$f_{p,p} = - \frac{m_p}{\rho_g} \nabla p \quad (12)$$

As every particle interacts during the transport with the surrounding gas-phase, the rotational (angular) momentum is transported by the particle–fluid interface and is defined as

$$\frac{d}{dt} \omega_p = t_{p,g} \quad (13)$$

where ω_p is the angular velocity of particle, and $t_{p,g}$ is the torque from gas-phase acting on the particle. The exerted torque

Table 1 Overview of numerical experiments performed in this study including atmospheric and fan power conditions at two different altitudes

Experiments (#)	Altitude (ft)	Pressure ^a (Pa)	Temp. (K) ^a	Fan speed ^b (%)
1	10,000	69,700	268	Low
2	10,000	69,700	268	Medium
3	10,000	69,700	268	High
4	35,000	23,800	219	Low
5	35,000	23,800	219	Medium
6	35,000	23,800	219	High

^aParameters from International Standard Atmosphere (ISA) table (Standard Atmosphere, ISO 2533:1975)

^bLow, Medium, and High refer to 35, 75, and 90% of maximum fan speed, respectively.

$$t_{p,g} = \frac{\mu_g}{64I_g} D_p^3 C_R \Omega_p Re_R \quad (14)$$

can be calculated using the drag coefficient of rotation ($C_R = 64\pi/Re_R$), that depends on the particle rotational Reynolds number ($Re_R = \rho_g D_p^2 |\omega_p| / \mu_g$), the particle fluid rotation velocity (Ω_p), that describes the difference between the particle and fluid velocity on the particle surface, and the inertia of a spherical particle ($I_p = m_p D_p^2 / 10$) [41].

In addition to the translational force balance and the rotational momentum balance, we also considered the influence of instantaneous turbulent velocity fluctuations (turbulent local disturbances, i.e., eddies, to the Reynolds-averaged gas-phase field) on the trajectories of the particles traversing through the precalculated turbulent flow field. We used a discrete random walk model [42], where the influence of instantaneous turbulent velocity fluctuations on the particle drag changes, as the particle movement increases with decreasing particle Stokes number ($Stk_p = \text{particle relaxation time/eddy lifetime}$). To fully capture the turbulent fluctuations of particle trajectories, we modeled a statistically large enough number of VA particle.

2.3 Experimental Setup. To investigate the probability of VA particle–fan interactions and resulting core entry concentrations, we first performed six individual flow field experiments (see Table 1). We considered two different flight altitudes (10,000 and 35,000 ft) and thus different atmospheric conditions (e.g., atmospheric pressure, temperature), chosen as the majority of ash clouds affecting aviation were found between 10,000 and 35,000 ft [11]. For each altitude, we simulated three fan power conditions, i.e., low, intermediate and high power, representing 35%, 75%, and 90% of full fan power (maximal rotational rates of the fan). All other parameters such as flight speed (inflow and outflow conditions), atmospheric temperature, and pressure were adjusted according to the individual flight phase and altitude. To reproduce realistic core intake conditions, we used an interface section at the core inlet with adjustable mass flow rates as well as adjustable total pressure and total temperature ratios.

Based on these six flow fields, we performed several particle-tracking experiments. The VA particles were assumed to be spherical, rigid, and internally homogeneous solid particles with a constant mass density of $\rho_p = 2700 \text{ kg/m}^3$, representing the most frequent volcanic ash type (andesitic volcanic ash) [19]. The particles were seeded from a 1.4 m × 1.4 m injector grid, with 20 equidistant grid points in each direction (400 injector points). The injector grid was located 6 m in front of the engine intake. The position and the size of the injector grid were adjusted to be comparable with engine test rig positions and numerical sensitivity tests were performed for individual dimensions and distances.

The initial particle conditions such as the particle velocity, , and external forces were interpolated from the gas-phase flow field location of the seeding points and no initial particle conditions were added to the injector grid. At each injector point, we

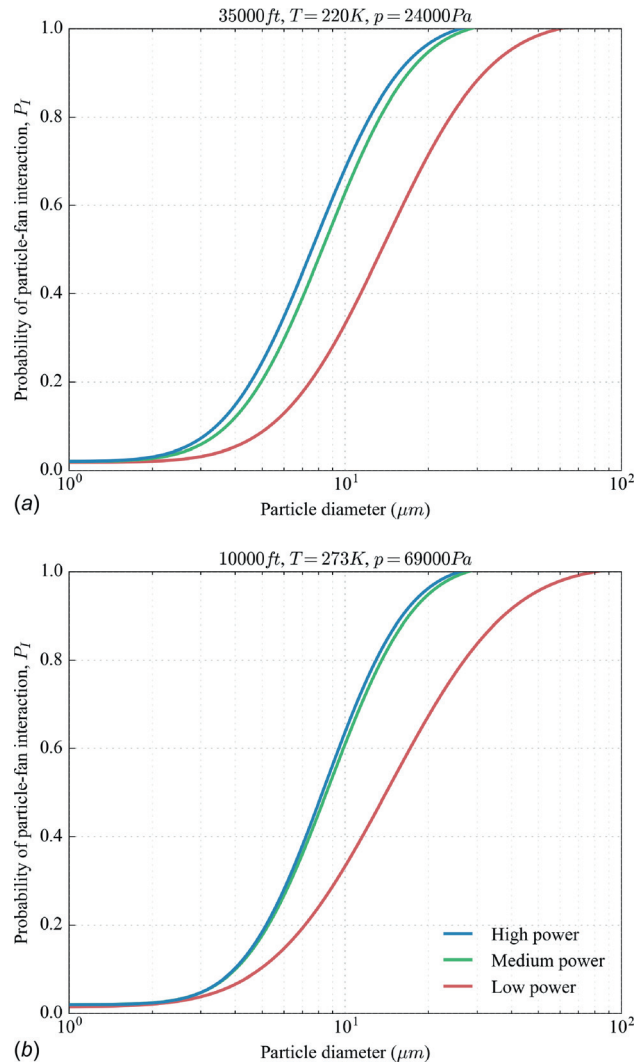


Fig. 5 Probability of particle–fan interaction (P_I) as a function of injected VA particle diameter (size range between 1 and 100 μm) for flight conditions at altitudes of (a) 35,000 ft and (b) 10,000 ft and for three different fan rotation rates (high power in blue, medium power in green, low power in red)

injected 1000 particles that ensured a statistically robust solution that is independent of the particle number. Simulations were carried out for 16 size bins from 1 to 100 μm . This resulted in a total number of 4×10^5 particles for each single particle size bin. To remove the fluctuations between the 16 size bins, we applied a least-squares minimization scheme for data fitting.

The interaction of particles with engine surfaces was captured by the use of a particle rebound (or bounce-off) wall collision model. This model assumes an ideal, smooth surface, where the momentum loss during a particle–wall interaction is described as the ratio of the particle velocity before and after impact. The rebound velocity, divided into normal ($u_{t,a} = e_t u_{t,b}$) velocity components, was calculated using constant user defined (normal and tangential) restitution coefficients (e_n and e_t). In this setup, VA particles are assumed to have a perfect elastic response, $e_n, e_t = 1$, meaning that the particles rebound back (energy transfer without losses) into the domain and do not break up after impact.

3 Results of Particle-Tracking Experiments

3.1 Probability of Particle–Fan Interaction. The probability of particle–fan interaction (P_I) as a function of volcanic ash particle size is shown in Fig. 5. The three lines represent low

Table 2 Probability of particle–fan interaction, P_I , as a function of particle diameter for seven VA relevant sizes and for both altitudes

Diameter (μm)	Probability of particle–fan interaction, P_I (%)					
	35,000 ft			10,000 ft		
	Low power	Medium power	High power	Low power	Medium power	High power
1	1.46	2.00	2.03	0.54	0.74	1.20
5	21.9	20.3	24.5	20.8	35.1	36.1
10	42.2	62.9	68.4	41.1	62.7	63.8
20	67.7	94.7	96.5	66.7	87.2	87.2
50	94.4	100	100	93.9	99.7	99.7
63	97.5	100	100	97.1	100	100
100	99.8	100	100	99.6	100	100

power (red), medium power (green) and high power (blue) fan rotation rates, and the two figure panels illustrate results for two different flight altitudes: (a) 35,000 ft and (b) 10,000 ft. All six cases (low, medium and high power at 35,000 ft and 10,000 ft) show that the probability of particle–fan interaction is clearly dependent on particle size and therefore on their individual Stokes number. For all fan rotation rates, particles with a diameter of 1–2 μm ($\text{Stk} \ll 1$) do not often interact with any of the fan surfaces ($P_I < 5\%$). For particles $\geq 2 \mu\text{m}$, the probability of particle–fan interaction starts to be different between the different fan rotation rates. Conditions at medium and high power result in similar particle–fan interaction probabilities, with slightly higher values at high power, where fewer interactions occur at low fan power. Interactions at the two altitudes are also similar, but generally, particles $< 20 \mu\text{m}$ show a higher interaction probability at 35,000 ft than at 10,000 ft, whereas particles $> 20 \mu\text{m}$ have nearly identical interaction probabilities. $P_I = 0.5$ is reached between 7 and 13 μm for all power conditions and altitudes and $P_I = 1.0$ at $\sim 63 \mu\text{m}$ (upper size of the fine fraction of volcanic ash). It is important to note that particles that interact with a surface can enter the engine core section. However, the probability strongly decreases with increasing VA particle size. An overview of the particle–fan interaction probability for seven relevant VA sizes is shown in Table 2.

To illustrate the particle interactions with the fan, we show example trajectories for four different VA particles sizes at medium fan power and at 35,000 ft (Fig. 6). The particle sizes were used to demonstrate the particle fraction with $\text{Stk} \ll 1$ (1 μm), a particle fraction with $\text{Stk} \sim 1$ (10 and 20 μm), and a particle fraction with $\text{Stk} \gg 1$ (63 μm , upper limit of the fine fraction of volcanic ash). The four particle sizes were all seeded from a single grid point on the injector grid with a total number of ten particles

per size class. Taking the 1 μm particles (blue dots), with almost no interaction with the surface, as a reference to indicate the flow streamline (perfect advection), it can be seen that the 10 μm particles (green dots) are slightly detached from this pathway, but still end up in the same fan stage passage (between a blade pair). However, they have already more particle–fan interactions ($P_I = 0.5$). The 20- μm sized particles (yellow dots) reveal a larger degree of detachment from the airflow and have even more contact with the surface (i.e., leading edge of the fan blade, $P_I = 0.85$). Finally, the 63 μm sized particles (red dots) are fully detached from the airflow and end up in a completely different fan blade passage with $P_I = 1.0$.

The individual particle impact positions on the fan surface show that most of the interactions occur at the leading edges, blade tips and the pressure surface. From these interactions, larger particles tend to be more deflected (due to their higher inertia and resulting radial acceleration), and therefore be centrifuged outward into the bypass flow of the engine. This leads to changes in particle trajectories from the core stream flow into the bypass flow and therefore to a reduction of the core stream flow mass concentration. Generally, the example shows that small particles (1 and 10 μm) are transported into the core region of the engine without being much deflected, whereas a large fraction of the large particles (20 and 63 μm) is transported from the core stream flow into the bypass stream flow after colliding with a surface (Fig. 6(b)).

3.2 Core Reduction Factors. As a result of the VA particle–fan interactions and thus particle transport from the core flow into the bypass flow, we also investigated the size-dependent VA particle reduction inside the core flow. The VA particle reduction is expressed by a size-dependent reduction factor

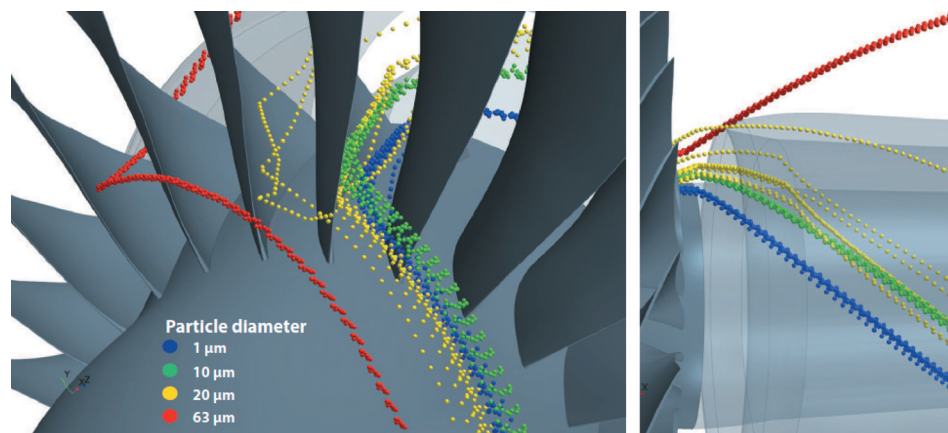


Fig. 6 Example particle trajectories of four relevant VA particle size classes (1 μm , 10 μm , 20 μm , and 63 μm), all released from the same injector grid point for illustration of size-dependent particle–fan interactions and showing the centrifuging effect

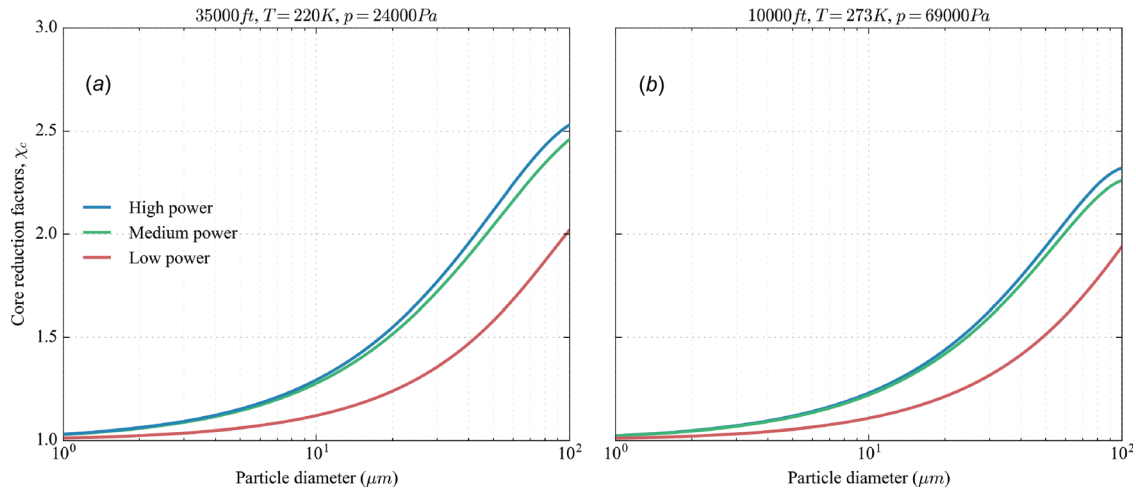


Fig. 7 Simulated core stream reduction factors (χ_c) for (a) 35,000 ft and (b) 10,000 ft altitudes as a function of fan rotation rates and VA particle diameter (μ). The colored lines represent the low power (red), medium power (green) and high power (blue) condition of the fan.

$$\chi_c(D_p) = \frac{n(D_p)_i}{n(D_p)_c} \quad (15)$$

that is defined as the particle size-dependent ratio of the initial particle number inside the core streamflow in front of the fan stage ($n(D_p)_i$) (i.e., in the atmosphere) and after the fan stage, thus inside the engine core ($n(D_p)_c$). The core reduction factor (χ_c) at two altitudes and three rotating rates and as a function of particle diameter is plotted in Fig. 7. In case of no particle–fan interaction, the core reduction factor is 1, meaning that the total number of incoming particles is equal to the particle number inside the engine core section. The results show that particles with a diameter of $\sim 1 \mu\text{m}$, at both altitudes and all engine operation conditions, are almost not affected by the fan and stay inside the core (Figs. 5 and 6). Therefore, particles of this size find their way into the engine core without interacting with fan blade surfaces. Higher fan power conditions (blue lines) and larger particles, as shown by the particle–fan interaction experiments (Fig. 5), lead to a higher frequency of particle collisions with the fan or the spinner and therefore to an increased deflection of particles from the core stream flow into the bypass stream flow. This is mainly influenced by the high initial inertia of large particles with a large Stokes number. The core reduction factors for the largest simulated particles in this study ($100 \mu\text{m}$ diameter) resulted in $\chi_c = 2.53$ for the high power condition and $\chi_c = 2.02$ for the low power condition at 35,000 ft and in $\chi_c = 2.32$ for the high power condition and $\chi_c = 1.94$ for the low power condition at 10,000 ft.

4 Discussion

4.1 Impact of χ_c on Generic Volcanic Ash Mass Concentrations. To calculate the particle mass concentration reduction inside the core streamflow, we applied the core reduction factors (χ_c) to generic atmospheric probability density functions (PDF) of VA concentrations in the size range between 1 and $100 \mu\text{m}$. The PDFs were generated using the same logarithmic standard deviation ($\sigma = 1.7$) for all PDFs, but different mean diameter (μ) ranging between 1 and $16 \mu\text{m}$, with an interval of $1 \mu\text{m}$ (16 PDFs) as reported by Prata and Prata [43]. Differences in μ can be related to the distance between a potential volcanic ash cloud encounter and the eruption source, where smaller particle size distributions (smaller μ) represent distal volcanic ash and larger particle size distributions (larger μ) represent proximal

volcanic ash. The mass concentration inside the core flow region is defined as

$$M_{p,\text{core}} = \int_{D_{p,\text{min}}}^{D_{p,\text{max}}} \rho_p D_p^3 \frac{\pi}{6} \left(\frac{n(D_p)_i}{\chi_c(D_p)} \right) dD_p \quad (16)$$

where the particle mass of a single particle ($m_p = \rho_p D_p^3 \pi / 6$) is multiplied by the total number of particles of a given particle size in the size range between $D_{p,\text{min}} = 1 \mu\text{m}$ and $D_{p,\text{max}} = 100 \mu\text{m}$. For the mass concentrations calculation before (b) the fan, we used a constant core reduction factor of $\chi_c = 1$ (no reduction) and for the mass concentration after (a) the fan we used the core reduction factors presented in Sec. 3.2. Finally, from the two resulting mass concentrations, we calculated the mass concentration reduction ($dM_{p,\text{core}} = M_{p,\text{core},i} / M_{p,\text{core},c}$).

Figure 8 illustrates the change of four selected PDFs ($\mu = 2, 4, 8, \text{ and } 16 \mu\text{m}$) after applying the core reduction factors χ_c for a flight altitude of 35,000 ft, where the colored lines correspond to the three tested fan rotation rates and the black lines to the initial PDF. Panel (a) shows almost no difference between the initial PDF ($\mu = 2 \mu\text{m}$) and the resulting PDFs. The calculated VA particle mass concentration difference resulted in a reduction of 5.3%. The PDFs with a starting $\mu = 4 \mu\text{m}$ (Panel (b)) show already a reduction of particles in the engine core, mostly of larger particles, and therefore, a change in distribution. This resulted in a particle mass concentration reduction of 4.4% for the low power case, 9.5% for the medium power case and 10% for the high power case. Panel (c) shows $\mu = 8 \mu\text{m}$ with even higher changes in PDFs. The changes imply a shift toward smaller particles (skewed distributions), which result in a mass reduction of 8.3%, 16.6%, and 17.4% for the low, medium, and higher power cases, respectively. The largest changes, both in the shape of the PDFs, particle number, and the VA mass concentrations reduction, were observed for the largest tested mean diameter ($\mu = 16 \mu\text{m}$). The PDFs are clearly reduced in terms of maximum values and shifted to small particles. The calculated VA mass reduction is 14.8% for the low power case, 26.5% for the medium power case, and 27.6% for the high power case.

For all power conditions, the reduction of VA mass concentrations shows an exponential increase in mass concentration reduction with increasing mean VA diameter. Another observation from the dataset is that the VA mass concentration reduction of the high power cases is twice as high as for the low power case, which shows a nonlinear relation between the fan rotation rate and

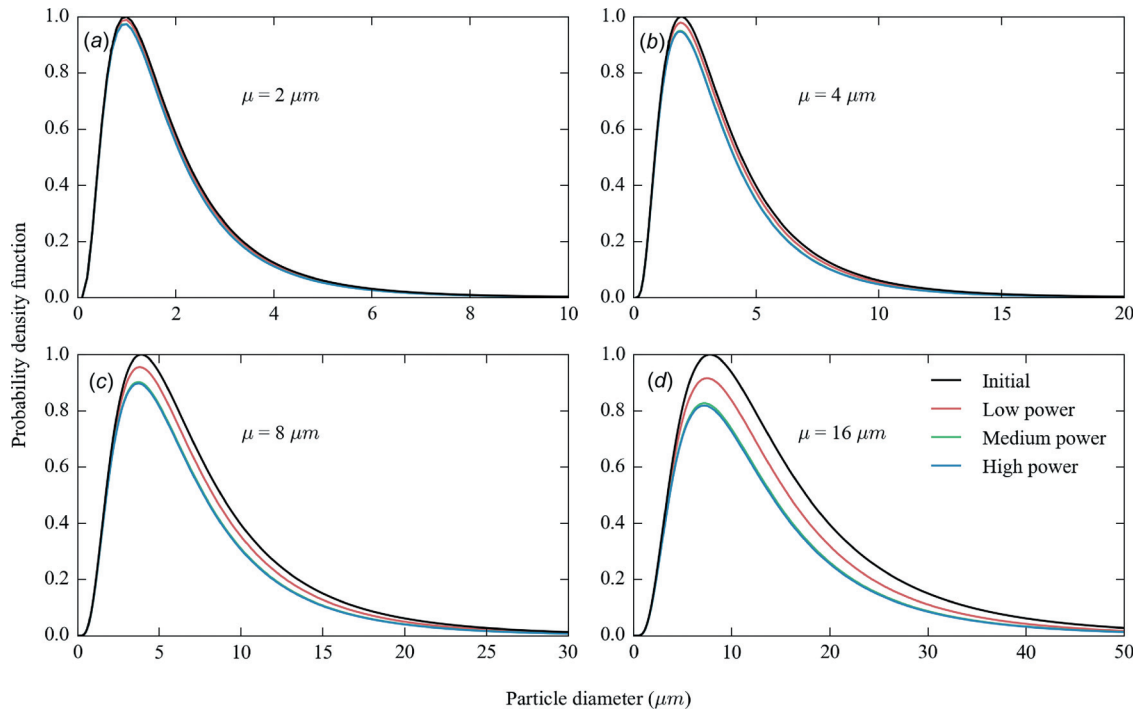


Fig. 8 Normalized generic PDFs of VA particle distributions for four selected median sizes. The black lines represent a potential atmospheric VA particle distribution and the colored lines the resulting core stream flow VA particle size distribution after applying the core reduction factors (χ_c) at flight altitude of 35,000 ft. All initial distributions have the same logarithmic standard deviation ($\sigma = 1.7$), which is a typical value for VA distributions.

Table 3 Mass concentration reduction of generic VA particle size distributions after applying the core stream flow factors (χ_c) and calculations of the mass concentration using a constant standard deviation ($\sigma = 1.7$) and mass density

Mean diameter D_p (μm)	VA mass reduction, $dM_{p,\text{core}}$ (%)		
	Low power	Medium power	High power
1.00	1.06	2.53	2.67
2.00	2.20	5.07	5.34
3.00	3.30	7.39	7.78
4.00	4.36	9.52	10.0
5.00	5.39	11.5	12.1
6.00	6.38	13.3	14.0
7.00	7.35	15.0	15.7
8.00	8.28	16.6	17.4
9.00	9.19	18.1	18.9
10.0	10.1	19.5	20.4
11.0	10.9	20.8	21.8
12.0	11.7	22.1	23.1
13.0	12.5	23.3	24.3
14.0	13.3	24.4	25.5
15.0	14.1	25.5	26.6
16.0	14.8	26.5	27.6

the mass reduction. Table 3 shows an overview of the calculated VA mass reductions for all PDFs and power conditions.

4.2 Case Study—Mt. Kelud Encounter 2014. To illustrate the effect of VA mass concentration reduction in the engine core due to the described particle–fan interactions, we applied the core reduction factors (χ_c) to atmospheric VA particle mass concentration distributions simulated for a real commercial aircraft VA encounter event [44]. The aircraft was en route from Perth, Australia, to Jakarta, Indonesia, when it accidentally encountered a dense volcanic ash cloud that was emitted by Mt. Kelud on the Feb. 13, 2014. The eruption was highly energetic and produced

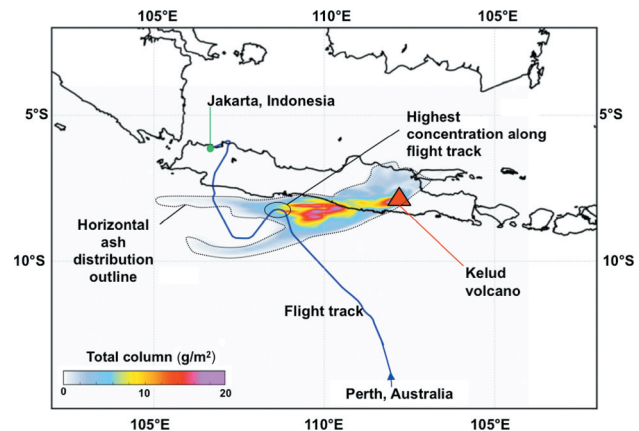


Fig. 9 Total VA columns simulated using the FLEXPART dispersion and transport model constrained with satellite observations. The blue line represents the flight track of the commercial aircraft traveling from Perth, Australia, to Jakarta, Indonesia, which encountered the ash cloud from the 2014 Mt. Kelud eruption (volcano is marked by the red triangle) (adapted from Ref. [17]).

an eruption column that reached altitudes of up to 16–17 km. The aircraft encountered a dispersed VA cloud at approximately 35,000 ft and during cruise flight conditions.

This encounter is described in more detail by Kristiansen et al. [17], who calculated temporal, spatial, and horizontal VA concentrations using an atmospheric dispersion model (FLEXPART [45]) that was constrained via an inverse modeling approach with VA particle satellite retrievals. From the model output, they extracted VA particle size and mass distributions along the flight track of the aircraft (Fig. 9). Their virtual flight through the simulated ash concentration field (blue line) shows that the modeled VA mass concentrations reached maximum concentrations of

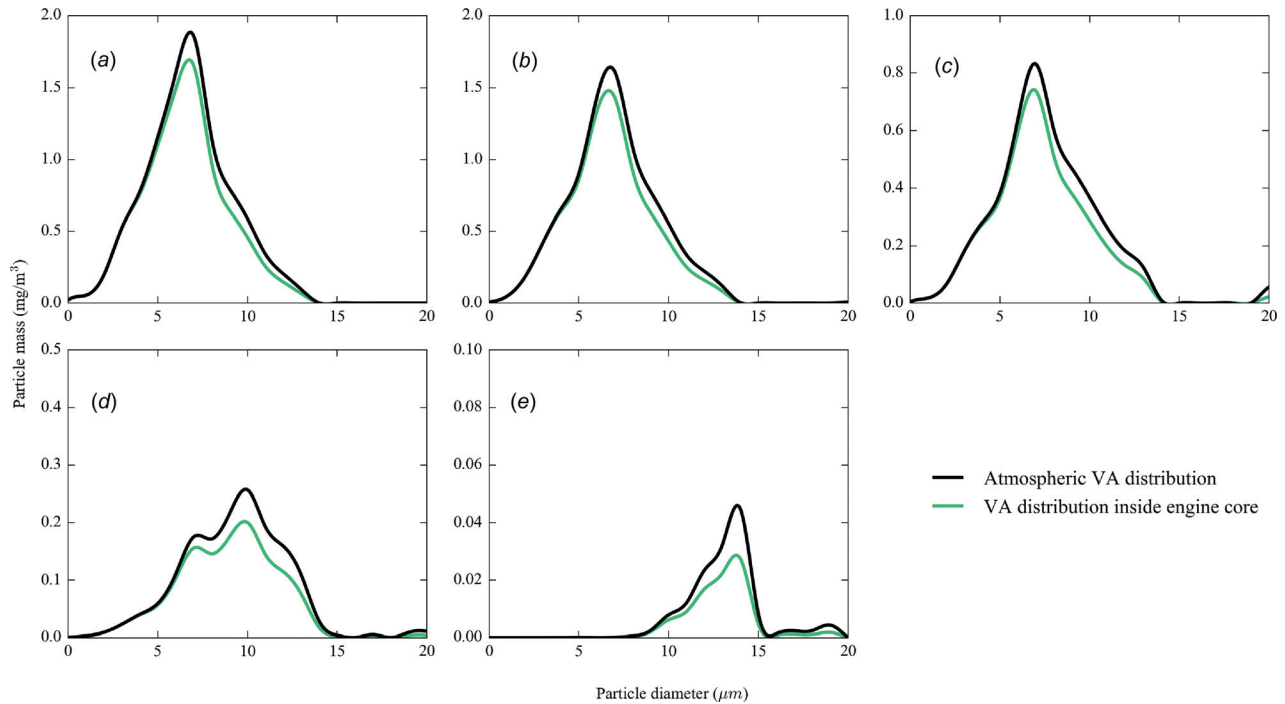


Fig. 10 Particle mass distributions of five consecutive minutes of the highest encountered concentrations inside the ash cloud (out of a total duration of 10 min) along the flight track shown in Fig. 9. The black solid lines represent the VA mass distributions in the atmosphere (extracted from the atmospheric dispersion model) and the green lines the corresponding VA mass distribution inside the engine core after applying our core reduction factors (χ_c) at 35,000 ft and medium power. The different panels represent 60 s averaged mass distributions inside the cloud, respectively.

$9 \pm 3 \text{ mg/m}^3$, with a mean concentration of $2 \pm 3 \text{ mg/m}^3$ over a total exposure time of 10 min, resulting in a total dosage of $1.2 \pm 0.3 \text{ g/m}^3$. The particle density in their study was set to 2500 kg/m^3 , very similar to the density used in our CFD setup (2700 kg/m^3).

Figure 10 shows VA particle mass distributions as a function of particle diameter along the flight track of the aircraft extracted from the dispersion model (black lines) and particle mass distribution after applying the core reduction factors (green lines) to the atmospheric data. The green lines represent, therefore, the engine core flow mass concentration that enters the engine core section. For these calculations, we applied the core entry factors of the 35,000 ft flight altitude and medium fan power condition case (Fig. 4(a), green line). For simplicity, we focused only on 5 min with the consecutive highest mass concentration during the encounter (minutes 2–6 inside the ash cloud).

The calculated mass reductions of the first 3 min are between 13.9% and 19.6%, whereas the mass reduction for the last 2 min is up to 34.9%. This can mainly be explained by the large atmospheric mean diameter of 10.5 and $20.2 \mu\text{m}$ of minutes 5 and 6 and thus larger influence of the core reduction factors. For the first 3 min (panels a–c)) the reduction of the mean diameter was calculated to be $0.35 \mu\text{m}$, whereas the mean diameter reduction for the

minutes 5 and 6 (panels d and e) was calculated to be $0.55 \mu\text{m}$. The calculated mass reductions show a good agreement with the impact analysis using generic volcanic ash mass concentrations as presented in Sec. 4.1. Furthermore, the separation of particles by the fan resulted in a dosage reduction inside the engine core flow of 12.3% (0.18 g/m^3) for the 5 min. An overview of the total atmospheric concentrations and resulting core entry concentrations, together with the corresponding mass concentration reductions are given in Table 4.

4.3 Limitations of Numerical Model and Results. In this study, we considered spherical particles. Assuming a different particle shape would imply a change of the drag coefficient of the particles. Various studies, e.g., Refs. [19] and [46], show that volcanic ash particles in the size range between 1 and $100 \mu\text{m}$ have a nonspherical shape, but the VA specific sphericity factors range between 0.75 and 0.9 (where 1 would be perfectly spherical). This means that the change of drag coefficient would be relatively small compared to spherical particles. This, in combination with very high velocities inside the engine intake, would have only a minor influence on the particle–fan interactions and therefore only a minor influence on the particle separation between the core stream flow and the bypass flow.

Table 4 Volcanic ash total atmospheric concentrations (based on model calculation and satellite observations [17]) and resulting core entry concentrations (after applying the core entry factors), together with the corresponding mass concentration reductions, for the 5 min of the flight with the highest VA concentrations during the 2014 Mt. Kelud ash cloud encounter case.

Time inside cloud (Min)	Encountered mean atmospheric particle size (μm)	Atmospheric mass concentration (mg/m^3)	Core stream flow mass concentration (mg/m^3)	VA mass reduction (%)
2	6.11	9.36	8.06	13.9
3	6.40	8.36	7.15	14.5
4	7.25	4.40	3.73	16.6
5	10.5	1.59	1.24	22.0
6	20.2	0.14	0.09	34.9

Another potential limitation of this setup is the particle–wall interaction model (Sec. 3.2). The model assumes that the particles do not break up after colliding with the fan surface and that they have a perfect rebound behavior. The particle–surface interaction as well as particle fragmentation are highly complicated processes and are part of ongoing research. Volcanic ash particles have a complex mineral structure, different microstructural phases and a significant glass content (often 50%) and have unknown fracture toughness. It is not clear if and how the particles break up after colliding with a surface (e.g., the fan blade). Generally, the larger the VA particles are, the higher is the probability of particle fragmentation due to a higher likelihood of structural defects in larger particles, but it is unclear at which particle size the structural defects start to form. Even if a single particle breaks into a larger number of smaller fragments, the generated kinetic energy from the high fan rotating speed acting on the fragments can still be large enough to transport (centrifuge) the fragments from the core stream flow into the bypass flow, which would have the same effect as without particle breakup. However, more research and experimental test data are required to fully understand the breakup mechanism and postbreakup behavior of VA particles in an aircraft engine. Still, we assume that particle break-up would not affect our overall conclusion that VA concentrations in the engine core are substantially reduced by centrifugal effects.

The particle–fan interaction as well as the core reduction experiments only considered three different fan rotation rates. The rates were chosen to represent relevant flight conditions. Additional investigations at power conditions above the high power (i.e., full power), between medium and low power (e.g., 50%) and below low power (i.e., idle) could extend our results. Since the difference between the medium and the high power case is only marginal, we believe that the full power condition would not be substantially different from the high power case. However, for conditions below the low power case, the interactions, and thus, the particle reductions could be less pronounced as at low power.

The presented results are representative of a large number of engine types and configurations. However, the current development to build engines with lower noise levels and lower specific fuel consumptions lead to a slower rotating fan and fewer fan blades. This development would lead to a reduced particle–fan interaction probability compared to current engine designs, leading to smaller reduction factors.

Furthermore, it is important to note that our results are valid also for other important atmospheric particle types (e.g., mineral dust) with a similar size range and mass density as the investigated VA particles.

5 Summary and Conclusions

In this study, we investigated volcanic ash particle ingestion into a representative engine, powering current wide-body aircraft, for three different fan power conditions and two different flight altitudes. We used a numerical CFD particle-tracking model to calculate particle–fan interactions as a function of various volcanic ash particle sizes. From the numerical simulations, we obtained engine core reduction factors for VA particles entering the engine core, which quantify the reduction of the atmospheric VA concentration due to centrifugal effects by the fan, as the particle-laden airflow enters the core stream flow. We applied the size-dependent core reduction factors first to generic VA size distribution probability density functions to calculate mass concentration reductions and then to a real volcanic ash cloud encounter event (Mt. Kelud 2014).

The particle–fan interaction results, and thus the obtained engine core reduction factors, clearly show for the first time the significant influence of the fan on ingested volcanic ash particles. The numerical experiments confirm the hypothesis that the fan acts like a volcanic ash particle separator. The results illustrate that particles $< 2 \mu\text{m}$ do not often interact with the fan surfaces (probability $< 5\%$), but more interactions occur for larger

particles. The interaction probability is also strongly dependent on the rotation speed of the fan. The highest investigated fan power, 90% of full power, resulted in a 100% interaction probability for VA particles larger than $63 \mu\text{m}$, which represents the upper size of the fine fraction of VA. The largest VA particle diameter ($100 \mu\text{m}$) and the highest fan power condition (high power) in this study resulted in a maximum core reduction factor of $\chi_c = 2.53$ at 35,000 ft.

Calculations of the mass reduction after applying the engine core reduction factors to generic probability density functions of different mean diameter show that for a given generic atmospheric VA size distribution, the reduction of VA mass concentrations is significant for size distributions with a mean diameter of $3 \mu\text{m}$. The calculations also show an exponential reduction with increasing particle size. Furthermore, the mass reduction shows the substantial impact of the fan on engine core exposure calculations (core entry exposure and dosage), where traditionally only atmospheric VA mass concentration data were considered. The maximum potential particle mass concentration reduction was calculated to be up to 30% for a generic particle density function with a mean diameter of 16 concentrations is significant for size distributions with a mean diameter of $3 \mu\text{m}$. The calculations of the generic distribution also confirm the mass reduction calculations of the real VA particle encounter (Mt. Kelud eruption 2014), where the VA particle mass concentration reduction (estimated using a combined atmospheric dispersion model and satellite approach) was calculated to be $\sim 30\%$.

The presented results show that the fan has a significant influence on the ingested particle distribution and ultimately on the mass concentration inside the engine core section. This knowledge will be crucial for future VA encounters, to relate atmospheric VA mass concentrations and particle size distributions to potential damage inside the engine core section (i.e., erosion rates, tip clearance growth, melting behavior of particles inside the combustion chamber, and adhesion of VA material). Furthermore, the presented data can be used to calculate the engine core relevant dose rate, exposure, and/or dosage needed to calculate their impact on the operability of aero engines and to assess their potential safety risk. Combined with calculations of atmospheric VA exposure and dosages along flight routes [30], this would allow judging the VA threat to engine cores much more reliably in the future.

Acknowledgment

A. Vogel was fully supported by the VERTIGO (Volcanic ash: field, experimental and numerical investigations of processes during its lifecycle) Marie Curie Initial Training Network, funded through the European Seventh Framework Program (FP7 2007–2013) under grant agreement number 607905. The work of M. Cassiani and A. Stohl was supported by the European Research Council (ERC) under the European Union's Horizon 2020 research and innovation program under grant agreement No. 670462 (COMTESSA). We greatly acknowledge the help and support of Nina Kristiansen, for the provision of the modeled dispersion as well as the exposure data along the flight track. Furthermore, we thank Rolls-Royce plc. for the provision of the engine geometries, the performance data and their technical support, especially the Fan and Compressor Aerodynamics group as well as the Installation Aero group. We also acknowledge Siemens PLM (former CD-Adapco) for their software and technical support that was substantial for the success of this study. The CFD simulations were performed on resources provided by UNINETT Sigma2—the National Infrastructure for High-Performance Computing and Data Storage in Norway.

Funding Data

- FP7 People: Marie-Curie Actions (607905).
- H2020 European Research Council (670462).

References

- [1] Casadevall, T. J., 1994, *Volcanic Ash and Aviation Safety: Proceedings of the First International Symposium on Volcanic Ash and Aviation Safety*, Vol. 2047, DIANE Publishing, Seattle, WA.
- [2] Prata, A. J., and Tupper, A., 2009, "Aviation Hazards From Volcanoes: The State of the Science," *Nat. Hazards*, **51**(2), pp. 239–244.
- [3] Guffanti, M., and Miller, T. P., 2013, "A Volcanic Activity Alert-Level System for Aviation: Review of Its Development and Application in Alaska," *Nat. Hazards*, **69**(3), pp. 1519–1533.
- [4] Rose, W. I., and Durant, A. J., 2009, "Fine Ash Content of Explosive Eruptions," *J. Volcanol. Geotherm. Res.*, **186**(1–2), pp. 32–39.
- [5] Self, S., and Walker, G. P., 1994, "Ash Clouds: Characteristics of Eruption Columns," *Volcanic Ash and Aviation Safety: Proceeding of the First International Symposium on Volcanic Ash and Aviation Safety*, United States Government Publishing Office, Washington, DC, pp. 65–74.
- [6] Carey, S., and Bursik, M., 2015, *Volcanic Plumes*, Wiley, London.
- [7] Guffanti, M., Mayberry, G. C., Casadevall, T. J., and Wunderman, R., 2009, "Volcanic Hazards to Airports," *Nat. Hazards*, **51**(2), pp. 287–302.
- [8] Miller, T., and Casadevall, T. J., 2000, *Volcanic Ash Hazards to Aviation*, Academic Press, San Diego, CA.
- [9] Stohl, A., Prata, A. J., Eckhardt, S., Clarisse, L., Durant, A., Henne, S., Kristiansen, N. I., Minikin, A., Schumann, U., Seibert, P., Stebel, K., Thomas, H. E., Thorsteinsson, T., Tørseth, K., and Weinzierl, B., 2011, "Determination of Time-and Height-Resolved Volcanic Ash Emissions and Their Use for Quantitative Ash Dispersion Modeling: The 2010 Eyjafjallajökull Eruption," *Atmos. Chem. Phys.*, **11**(9), pp. 4333–4351.
- [10] Oxford Economics, 2010, "The Economic Impacts of Air Travel Restrictions Due to Volcanic Ash," Abbey House, Oxford, UK, [Report](#).
- [11] Guffanti, M., Casadevall, T. J., and Budding, K., 2010, "Encounters of Aircraft With Volcanic Ash Clouds: A Compilation of Known Incidents, 1953–2009," US Geological Survey, Reston, VA, Data Series 545, Version 1, pp. 1–12.
- [12] Christmann, C., Nunes, R., Schmitt, A., and Guffanti, M., 2017, "Flying Into Volcanic Ash Clouds: An Evaluation of Hazard Potential," The North Atlantic Treaty Organization, Vilnius, Lithuania, p. 1028.
- [13] Przedpelski, Z. J., and Casadevall, T. J., 1994, "Impact of Volcanic Ash From 15 December 1989 Redoubt Volcano Eruption on GE CF6-80C2 Turbofan Engines," *Volcanic Ash and Aviation Safety: Proceedings of the First International Symposium on Volcanic Ash and Aviation Safety*, United States Government Publishing Office, Washington, DC, pp. 129–135.
- [14] Witham, C., Webster, H., Hort, M., Jones, A., and Thomson, D., 2012, "Modelling Concentrations of Volcanic Ash Encountered by Aircraft in past Eruptions," *Atmos. Environ.*, **48**, pp. 219–229.
- [15] Clarkson, R. J., Majewicz, E. J. E., and Mack, P., 2016, "A Re-evaluation of the 2010 Quantitative Understanding of the Effects Volcanic Ash Has on Gas Turbine Engines," *Proc. Inst. Mech. Eng. Part G: J. Aerosp. Eng.*, **230**(12), pp. 1–18.
- [16] Vernier, J.-P., Fairlie, T. D., Deshler, T., Natarajan, M., Knepp, T., Foster, K., Weinhold, F. G., Bedka, K. M., Thomason, L., Trepte, C., Wienhold, F. G., Bedka, K. M., Thomason, L., and Trepte, C., 2016, "In Situ and Space-Based Observations of the Kelud Volcanic Plume: The Persistence of Ash in the Lower Stratosphere," *J. Geophys. Res.: Atmos.*, **121**(18), pp. 104–118.
- [17] Kristiansen, N. I., Prata, A. J., Stohl, A., and Carn, S. A., 2015, "Stratospheric Volcanic Ash Emissions From the 13 February 2014 Kelut Eruption," *Geophys. Res. Lett.*, **42**(2), pp. 588–596.
- [18] Bagheri, G., and Bonadonna, C., 2016, "Aerodynamics of Volcanic Particles: Characterization of Size, Shape, and Settling Velocity," *Volcanic Ash*, Elsevier, Amsterdam, The Netherlands, Chap. 2.
- [19] Vogel, A., Diplas, S., Durant, A. J., Azar, A. S., Sunding, M. F., Rose, W. I., Sytchkova, A., Bonadonna, C., Krüger, K., and Stohl, A., 2017, "Reference Data Set of Volcanic Ash Physicochemical and Optical Properties," *J. Geophys. Res.: Atmos.*, **122**(17), pp. 9485–9514.
- [20] Tabakoff, W., Lakshminarasimha, A. N., and Pasin, M., 1990, "Simulation of Compressor Performance Deterioration Due to Erosion," *ASME J. Turbomach.*, **112**(1), p. 78.
- [21] Tabakoff, W. C., Hamed, A., and Metwally, M., 1991, "Effect of Particle Size Distribution on Particle Dynamics and Blade Erosion in Axial Flow Turbines," *ASME J. Eng. Gas Turbines Power*, **113**(4), p. 607
- [22] Corsini, A., Marchegiani, A., Rispoli, F., Venturini, P., and Sheard, A. G., 2012, "Predicting Blade Leading Edge Erosion in an Axial Induced Draft Fan," *ASME J. Eng. Gas Turbines Power*, **134**(4), p. 042601.
- [23] Kueppers, U., Cimarelli, C., Hess, K.-U., Taddeucci, J., Wadsworth, F. B., and Dingwell, D. B., 2014, "The Thermal Stability of Eyjafjallajökull Ash Versus Turbine Ingestion Test Sands," *J. Appl. Volcanol.*, **3**(1), p. 4.
- [24] Taltavull, C., Dean, J., and Clyne, T. W., 2016, "Adhesion of Volcanic Ash Particles Under Controlled Conditions and Implications for Their Deposition in Gas Turbines," *Adv. Eng. Mater.*, **18**(5), pp. 803–813.
- [25] Kim, J., Dunn, M. G., Baran, A. J., Wade, D. P., and Tremba, E. L., 1993, "Deposition of Volcanic Materials in the Hot Sections of Two Gas Turbine Engines," *ASME J. Eng. Gas Turbines Power*, **115**(3), p. 641.
- [26] Drexler, J. M., Gledhill, A. D., Shinoda, K., Vasiliev, A. L., Reddy, K. M., Sampath, S., and Pature, N. P., 2011, "Jet Engine Coatings for Resisting Volcanic Ash Damage," *Adv. Mater.*, **23**(21), pp. 2419–2424.
- [27] Mechnich, P., Braue, W., and Schulz, U., 2011, "High-Temperature Corrosion of EB-PVD Yttria Partially Stabilized Zirconia Thermal Barrier Coatings With an Artificial Volcanic Ash Overlay," *J. Am. Ceram. Soc.*, **94**(3), pp. 925–931.
- [28] Vidal-Setif, M. H., Chellah, N., Rio, C., Sanchez, C., and Lavigne, O., 2012, "Calcium-Magnesium-Alumino-Silicate (CMAS) Degradation of EB-PVD Thermal Barrier Coatings: Characterization of CMAS Damage on Ex-Service High Pressure Blade TBCs," *Surf. Coat. Technol.*, **208**, pp. 39–45.
- [29] Song, W., Lavallée, Y., Hess, K.-U., Kueppers, U., Cimarelli, C., and Dingwell, D. B., 2016, "Volcanic Ash Melting Under Conditions Relevant to Ash Turbine Interactions," *Nat. Commun.*, **7**, p. 10795.
- [30] Prata, A. J., Kristiansen, N. I., Thomas, H. E., and Stohl, A., 2018, "Ash Metrics for European and trans-Atlantic Air Routes During the Eyjafjallajökull Eruption 14 April–23 May, 2010," *J. Geophys. Res.: Atmos.*, **123**(10), pp. 5469–5483.
- [31] Weaver, M. M., Dunn, M. G., and Heffernan, T., 1996, "Experimental Determination of the Influence of Foreign Particle Ingestion on the Behavior of Hot-Section Components Including Lamilloy," *ASME Turbo Expo*, **66**(3), pp. 911–917.
- [32] Brennen, C. E., 2005, *Fundamentals Multiphase Flows*, Cambridge University Press, Cambridge, UK.
- [33] Siemens PLM Software, 2016, "*Star-CCM+ v11*," Siemens PLM Software, London.
- [34] Lee, D. T., and Schachter, B. J., 1980, "Two Algorithms for Constructing a Delaunay Triangulation," *Int. J. Comput. Inf. Sci.*, **9**(3), pp. 219–242.
- [35] Baker, T. J., 2005, "Mesh Generation: Art or Science?," *Prog. Aerosp. Sci.*, **41**(1), pp. 29–63.
- [36] Elghobashi, S., 1994, "On Predicting Particle-Laden Turbulent Flows," *Appl. Sci. Res.*, **52**(4), pp. 309–329.
- [37] Shih, T.-H., Liou, W., Shabbir, A., Yang, Z., and Zhu, J., 1994, "A New k-Epsilon Eddy Viscosity Model for High Reynolds Number Turbulent Flows—Model Development and Validation," National Aeronautics and Space Administration, Cleveland, OH, Report No. [NASA-TM-106721](#).
- [38] Wolfshtein, M., 1969, "The Velocity and Temperature Distribution in One-Dimensional Flow With Turbulence Augmentation and Pressure Gradient," *Int. J. Heat Mass Transfer*, **12**(3), pp. 301–318.
- [39] Kandhai, D., Derksen, J. J., and Van den Akker, H. E. A., 2003, "Interphase Drag Coefficients in Gas Solid Flows," *AIChE J.*, **49**(4), pp. 1060–1065.
- [40] Schiller, L., and Naumann, A., 1935, "A Drag Coefficient Correlation," *Z. Des Ver. Dtsch. Ing.*, **77**, pp. 318–320.
- [41] Rubinow, S. I., and Keller, J. B., 1961, "The Transverse Force on a Spinning Sphere Moving in a Viscous Fluid," *J. Fluid Mech.*, **11**(3), pp. 447–459.
- [42] Gosman, A. D., and Ioannides, E., 1983, "Aspects of Computer Simulation of Liquid-Fueled Combustors," *J. Energy*, **7**(6), pp. 482–490.
- [43] Prata, A. J., and Prata, A. T., 2012, "Eyjafjallajökull Volcanic Ash Concentrations Determined Using Spin Enhanced Visible and Infrared Imager Measurements," *J. Geophys. Res. Atmos.*, **117**(D20), pp. 1–24.
- [44] EASA, 2014, "Explanatory Note to ED Decision 2014/027/R and Comment-Response Document 2012-21," European Aviation Safety Agency, Cologne, Germany.
- [45] Stohl, A., Forster, C., Frank, A., Seibert, P., and Wotawa, G., 2005, "Technical Note: The Lagrangian Particle Dispersion Model FLEXPART Version 6.2," *Atmos. Chem. Phys. Discuss.*, **5**(9), pp. 4739–4799.
- [46] Wilson, L., and Huang, T. C., 1979, "The Influence of Shape on the Atmospheric Settling Velocity of Volcanic Ash Particles," *Earth Planet. Sci. Lett.*, **44**(2), pp. 311–324.